

Catalysis

Non-oxidative Methane Coupling over Silica versus Silica-Supported Iron(II) Single Sites

Petr Šot,^[a] Mark A. Newton,^[a] Dirk Baabe,^[b] Marc D. Walter,^[b] Alexander P. van Bavel,^[c] Andrew D. Horton,^[c] Christophe Copéret,^{*[a]} and Jeroen A. van Bokhoven^{*[a, d]}

Abstract: Non-oxidative CH₄ coupling is promoted by silica with incorporated iron sites, but the role of these sites and their speciation under reaction conditions are poorly understood. Here, silica-supported iron(II) single sites, prepared via surface organometallic chemistry and stable at 1020 °C in vacuum, are shown to rapidly initiate CH₄ coupling at 1000 °C, leading to 15–22% hydrocarbons selectivity at 3–4% conversion. During this process, iron reduces and forms carburized iron(0) nanoparticles. This reactivity contrasts with what is observed for (iron-free) partially dehydroxylated silica, that readily converts methane, albeit with low hydrocarbon selectivity and after an induction period. This study supports that iron sites facilitate faster initiation of radical reactions and tame the surface reactivity.

Non-oxidative coupling of CH₄ (NOCM) is a one-step methane conversion process to higher hydrocarbons (Scheme 1), which circumvents the conventional two-step synthesis based on steam reforming and Fischer–Tropsch process.^[1] NOCM is highly endothermic, requiring high temperatures, which also thermodynamically favour the competing reaction methane decarbonization that yields H₂ and coke.^[2] While oxidative coupling of CH₄ avoids the latter process, oxidative conditions lead to the production of CO₂, resulting in low hydrocarbon yields.^[3] Recent reports suggested that highly dispersed metal sites improve the selectivity of NOCM to hydrocarbons, opening new opportunities.^[4]

Metal-exchanged zeolites, such as those based on molybdenum and iron can convert CH₄ into hydrocarbons under non-oxidative conditions, wherein the interplay between Brønsted sites, the pore system, and the metal site is crucial.^[5] However, the thermal instability of zeolites limits the temperature range within which they may be applied, preventing high conversions from being reached, spurring the interest to identify more thermally stable oxides. For example, a material prepared by melting of iron orthosilicate and quartz was reported to produce hydrocarbons with selectivity over 99% at 1000 °C.^[4b] This outstanding activity is ascribed to the formation of isolated Fe-sites, promoting the activation of CH₄ and yielding methyl radicals. Recent studies have reported similar outcomes, albeit with lower yields and the production of a broader spectrum of hydrocarbons, including C₂H₆ and C₃–C₅ hydrocarbons, along with the formation of iron carbide nanoparticles.^[4c–e] These observations contrast with those related to other iron(0) and iron oxide systems supported on silica or alumina, as well as bare supports, all of which predominately induce CH₄ decarbonization.^[6] The low selectivity toward hydrocarbons can originate from longer contact times, low metal dispersion, and a high ratio of surface area of the material to the void space in the reactor bed, all of which would favour the formation of coke.^[4c, 6]

These results imply that iron facilitates CH₄ activation; however, its structure and mechanistic role remain unclear. Similarly, the role of the support in the reaction is also ambiguous. We therefore reasoned that generating well-defined iron sites, by combining surface organometallic chemistry (SOMC)^[7] with thermolytic molecular precursors (TMPs),^[8] and complementing it with a detailed characterization would provide molecular insight into these complex systems. Indeed, recent studies have shown that this combined approach helps engineering well-defined surface species with tailored nuclearity and oxidation state. This method consists of grafting a molecular precursor on reactive surface sites, typically the isolated hydroxyl groups of a partially dehydroxylated high surface area oxide, followed by a thermolysis step that yields metal sites free of organic ligands.^[9] Some prominent examples related to the work described herein are isolated Cr^{III},^[10] Ga^{III}^[11] sites on silica that are highly productive in C₃H₈ dehydrogenation, and isolated Cu^{II}^[12] sites on alumina that selectively convert CH₄ to CH₃OH.


Here, we report the generation of isolated Fe^{II} sites on the surface of silica dehydroxylated at 1080 °C (SiO₂₋₁₀₈₀), using dimeric Fe^{II} tris(*tert*-butoxy)siloxide (**1**)^[13] as a molecular precursor. These sites are stable at temperatures above 1000 °C in

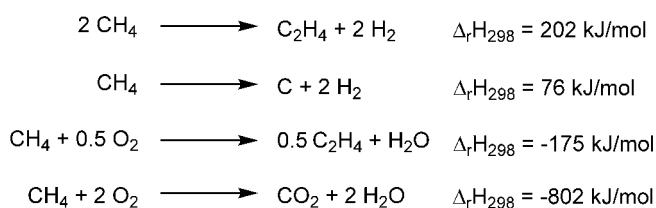
[a] Dr. P. Šot, Dr. M. A. Newton, Prof. Dr. C. Copéret, Prof. Dr. J. A. van Bokhoven
Department of Chemistry and Applied Biosciences
ETH Zürich, Vladimir-Prelog-Weg 1–5, 8093 Zürich (Switzerland)
E-mail: ccoperet@ethz.ch

[b] Dr. D. Baabe, Prof. Dr. M. D. Walter
Institut für Anorganische und Analytische Chemie
TU Braunschweig, Hagenring 30, 38106 Braunschweig (Germany)

[c] Dr. A. P. van Bavel, Dr. A. D. Horton
Shell Global Solutions International B.V.
Grasweg 31, 1031 HW Amsterdam (The Netherlands)

[d] Prof. Dr. J. A. van Bokhoven
Laboratory for Catalysis and Sustainable Chemistry
Paul Scherrer Institute, 5232 Villigen (Switzerland)
E-mail: jeroen.vanbokhoven@chem.ethz.ch

 Supporting information and the ORCID identification number(s) for the author(s) of this article can be found under:
<https://doi.org/10.1002/chem.202001139>.



Scheme 1. Conversion of CH₄ to C₂H₄ under non-oxidative and oxidative conditions, together with competing pathways.

the absence of reactive gas. Upon introduction of CH₄, the material initiates coupling and higher hydrocarbons are formed. This reactivity differs from SiO₂₋₁₀₈₀ that also activates CH₄, but with an induction period and lower selectivity towards hydrocarbons.

The molecular complex **1** was first grafted on SiO₂₋₁₀₈₀ (1 equiv. per surface OH group, see characterization in SI). This support, SiO₂₋₁₀₈₀, prepared by a vacuum treatment of Aerosil® 200 at 1080 °C, exhibits $n_{\text{OH}} = 0.08 \text{ mmol}_{\text{OH}} \text{ g}^{-1}$, $S_{\text{BET}} = 173 \text{ m}^2 \text{ g}^{-1}$ and $\theta_{\text{OH}} = 0.3 \text{ OH/nm}^2$. The grafting yields 1/SiO₂₋₁₀₈₀ with 0.7 wt% of iron and 3.5 wt% of carbon. Further treatment of 1/SiO₂₋₁₀₈₀ under vacuum at 1020 °C yields a white material (1/SiO₂₋₁₀₈₀)-₁₀₂₀, free of organic ligands and OH groups according to IR spectroscopy (Figure 1a). Contacting the sample with 60 mbar of CO leads to the formation of a band at 2160 cm⁻¹, consistent with presence of isolated iron(II) sites (Figure S2.7). The molar ratio between the deposited iron and surface OH is 1.6, suggesting grafting on strained siloxanes and/or formation of centres with higher nuclearity (dimers).^[14]

Table 1 lists the important properties of the studied materials. The Fe *K*-edge HERFD-XANES spectrum of (1/SiO₂₋₁₀₈₀)-₁₀₂₀ shows a weak two-component pre-edge, followed by an absorption edge at 7118.8 eV, consistent with the presence of Fe^{II} (Figure S2.2).^[15] EXAFS spectroscopy yields a spectrum with three scattering paths, namely, Fe–O, Fe–Fe and Fe–Si with coordination numbers of 1.8, 0.5 and 1.3 (Figure S2.4). The absence of any distant shells, along with the very low coordination number for Fe–Fe path rules out the formation of nanoparticles and is consistent with highly dispersed iron sites. Similarly, Fe *K*-edge of 1/SiO₂₋₁₀₈₀ is localized at 7119.7 eV, but is preceded by a weak pre-edge with three components. The EXAFS spectrum shows three scattering paths corresponding to Fe–O, Fe–Fe and Fe–Si with coordination numbers of 1.9, 0.5 and 1.3, respectively (Figure S2.4). These results also suggest that the spin state, oxidation state, and nuclearity of iron remains nearly unaffected before and after thermolysis, but that the symmetry does change. A comparison with the molecular precursor **1** reveals a loss of T_d symmetry and a decrease of coordination number upon grafting (Figure S2.2).

Zero-field ⁵⁷Fe Mössbauer spectroscopy shows significant differences between both samples (Figure S2.5 and see SI for details). The spectrum of (1/SiO₂₋₁₀₈₀)-₁₀₂₀ indicates the presence of two slightly different Fe^{II} high-spin sites with similar ratio and values for the isomer shift of $\delta = 0.97(4)$ and $0.80(3) \text{ mm s}^{-1}$, and quadrupole splitting of $\Delta E_Q = 0.94(6)$ and $1.06(5) \text{ mm s}^{-1}$, respectively. In contrast, the Mössbauer spectrum of 1/SiO₂₋₁₀₈₀ revealed two main components with isomer shifts of $\delta = 0.52(2)$ and $0.77(2) \text{ mm s}^{-1}$, and quadrupole splitting of $\Delta E_Q = 1.79(5)$ and $0.90(4) \text{ mm s}^{-1}$, respectively. These ob-

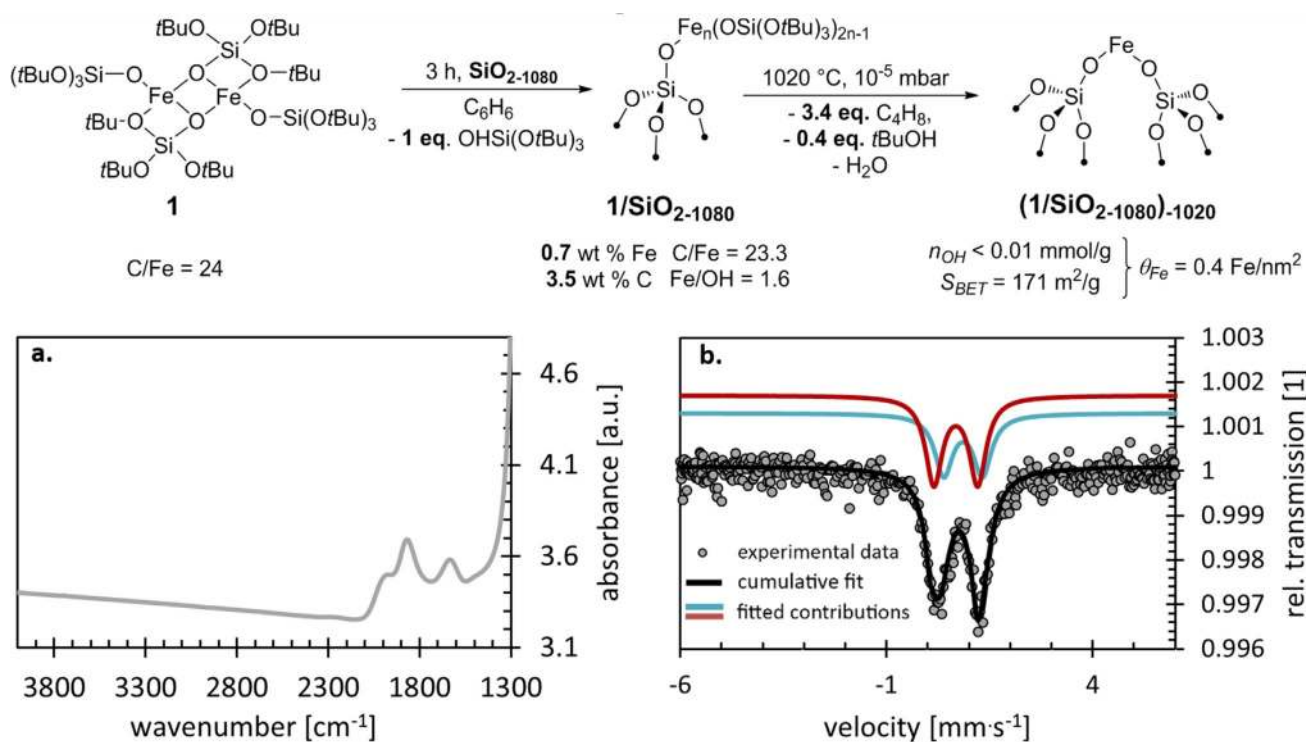


Figure 1. Synthesis of 1/SiO₂₋₁₀₈₀ and (1/SiO₂₋₁₀₈₀)-₁₀₂₀ from **1** and SiO₂₋₁₀₈₀ by grafting and thermolysis, including the basic characterization, (a) IR (a), and (b) zero-field ⁵⁷Fe Mössbauer spectrum of (1/SiO₂₋₁₀₈₀)-₁₀₂₀.

Table 1. Characteristic properties of 1, $1/\text{SiO}_{2-1080}$ and $(1/\text{SiO}_{2-1080})_{-1020}$ as detected by given analytic method.			
Analytic method	1	$1/\text{SiO}_{2-1080}$	$(1/\text{SiO}_{2-1080})_{-1020}$
IR spectroscopy ^[a]	confirms the structure and purity	loss of isolated O-H band, formation of C-H bands	removal of O-H and C-H bands CO sorption: Fe ^{II} sites
Fe K-edge XANES	oxidation state +II distorted T_d symmetry	oxidation state +II loss of T_d symmetry	oxidation state +II
Fe K-edge EXAFS	$N(\text{Fe}-\text{Fe})=1$ $N(\text{Fe}-\text{O})=4$	$N(\text{Fe}-\text{Fe})=0.5$ $N(\text{Fe}-\text{O})=2$	$N(\text{Fe}-\text{Fe})=0.5$ $N(\text{Fe}-\text{O})=2$
⁵⁷ Fe Mössbauer spectroscopy	oxidation state +II 1 Fe site (+ by-product) ^[b]	oxidation state +II 2 different Fe sites (+ by-product) ^[b]	oxidation state +II 2 similar Fe sites (+ no by-product)
SQUID magnetometry	high-spin Fe ^{II} paramagnetism (+ AF coupling or ZFS)	high-spin Fe ^{II} paramagnetism (+ AF coupling or ZFS)	high-spin Fe ^{II} paramagnetism + AF coupling or ZFS)

[a] See Figs S1.1, S2.7 in Supporting Information for more details. [b] minor (potentially hexa-coordinate) Fe^{II} species.^[13] See Figures S1.3, S2.5 in Supporting Information for more details.

servations are suggestive of the presence of two distinct Fe^{II} high-spin sites, again in a similar ratio, but with different coordination environments and bonding situations. The spin and oxidation state assignments for $1/\text{SiO}_{2-1080}$ and $(1/\text{SiO}_{2-1080})_{-1020}$ are further probed by solid-state magnetic susceptibility measurements (Figure S2.3 and see Supporting Information for details), also corroborating the formation of Fe^{II} high-spin centres in both compounds.

The reactivity of $(1/\text{SiO}_{2-1080})_{-1020}$ was evaluated and compared to SiO_{2-1080} under the following conditions: sample mass 100 mg, contact time 0.1 s, 7.5% of CH₄ in argon at atmospheric pressure and temperature 1000 °C. The samples were first heated under argon and after the target temperature was reached, the reactive gas was introduced. Figure 2a shows that $(1/\text{SiO}_{2-1080})_{-1020}$ immediately initiates the conversion of CH₄, but is followed by a rapid deactivation (1 min), after which the reaction proceeds at low-conversion (2–4%) with selectivity to hydrocarbons (C₂H₆, C₂H₄, C₂H₂ and C₆H₆) between 15–22%. The remaining part of the balance accounts mainly for production of carbon. For comparison, the reactivity of SiO_{2-1080} is shown in Figure 2b and highlights two different stages: following the induction period (t_i) of 35 min, during which no reaction occurs, the conversion of CH₄ rapidly increases to reach a value of 25%, with overall hydrocarbon selectivity of 5%, before slowly decreasing. Additional experiments establish a similar behaviour, but with somewhat varying t_i (Figure S3.1). This indicates that iron assists in the initiation of the reaction either directly, or by rapidly forming new reactive species. In contrast, the induction period observed with SiO_{2-1080} implies that the pure support is modified prior to initiating CH₄ coupling, which may be attributed to the reaction of CH₄ with silanols or the formation of different sites.^[6e,16]

The effect of contact time (Figure S3.2) on the conversion for both $(1/\text{SiO}_{2-1080})_{-1020}$ and SiO_{2-1080} further shows that SiO_{2-1080} reaches a higher conversion than $(1/\text{SiO}_{2-1080})_{-1020}$, indicating that the iron sites selectively suppress the surface reactivity towards CH₄. Figure 2c plots the dependency of selectivity to hydrocarbons on CH₄ conversion and shows comparable trends for both SiO_{2-1080} and $(1/\text{SiO}_{2-1080})_{-1020}$, including increased production of carbon at high conversion levels. Figures

3a and 3b compare the relative distribution of the hydrocarbons in the gas phase and show that at similar conversion ($1/\text{SiO}_{2-1080})_{-1020}$ produces higher fraction of C₂H₂ at the expense of C₂H₄, compared to SiO_{2-1080} , possibly attributed to the presence of iron.

STEM analysis of $(1/\text{SiO}_{2-1080})_{-1020}$ after the activity test at 1000 °C shows the formation of iron nanoparticles with $d=15$ –20 nm (Figures S4.1, S4.2), Fe K-edge XANES ascribes them oxidation state 0 and EXAFS reveals the presence of an extended carburized structure (Figure S4.3). A complementary in situ XAS study at lower temperature (800 °C) confirms a similar reduction phenomenon concomitant with iron nanoparticle formation (Figure S4.4). Powder X-ray diffraction further confirms these observations with a reflection at $2\theta=45.3^\circ$ and a shoulder at 44.5° , suggesting the presence of γ -iron and iron carbide (Figure S4.5).^[17] Formation of such species agrees with a phase diagram of Fe–C binary system.^[18] The support remains amorphous with a surface area of 170 m²g⁻¹ after oxidation of coke deposits. IR spectra recorded after three minutes on stream show the formation of three bands: $\nu(\text{O}-\text{H})$ at 3747 cm⁻¹, $\nu(\text{Si}-\text{H})$ at 2290 cm⁻¹ and $\nu(\text{C}=\text{C})$ at 1592 cm⁻¹ (Figure S4.6). The first two likely originate from opening of siloxane bridges by H₂ or CH₄, the last one belongs to coke. EPR measurement resolves a narrow resonance with $g_{\text{iso},1}=2.001$, and a broad one with $g_{\text{iso},2}=1.925$ (Figure S4.7). The former may belong to carbon or silicon radicals, but the assignment of the second peak is not straightforward. It might represent a resonance of ferromagnetic Fe⁰ nanoparticles or traces of a paramagnetic Fe^{III} impurity.^[19] For comparison, the EPR spectrum of SiO_{2-1080} during t_i , shows formation of a weak resonance at $g_{\text{iso}}=2.0033$ belonging to carbon radicals.^[20] Two minutes past t_i , the spectrum features a resonance at $g_{\text{iso}}=2.0048$ (Figure S4.8), indicating the evolution of the defects and that they are different to those formed in $(1/\text{SiO}_{2-1080})_{-1020}$. The IR spectrum recorded after three minutes of CH₄ consumption reveals the formation of a weak band $\nu(\text{Si}-\text{H})$ at 2290 cm⁻¹ (Figure S4.9), similarly to $(1/\text{SiO}_{2-1080})_{-1020}$. It is noteworthy that Fe⁰, hydrosilanes, carbonaceous materials, and Si defects are all known to activate CH₄ or olefins, complicating the deconvolution of their effects on the overall activity.^[6,21]

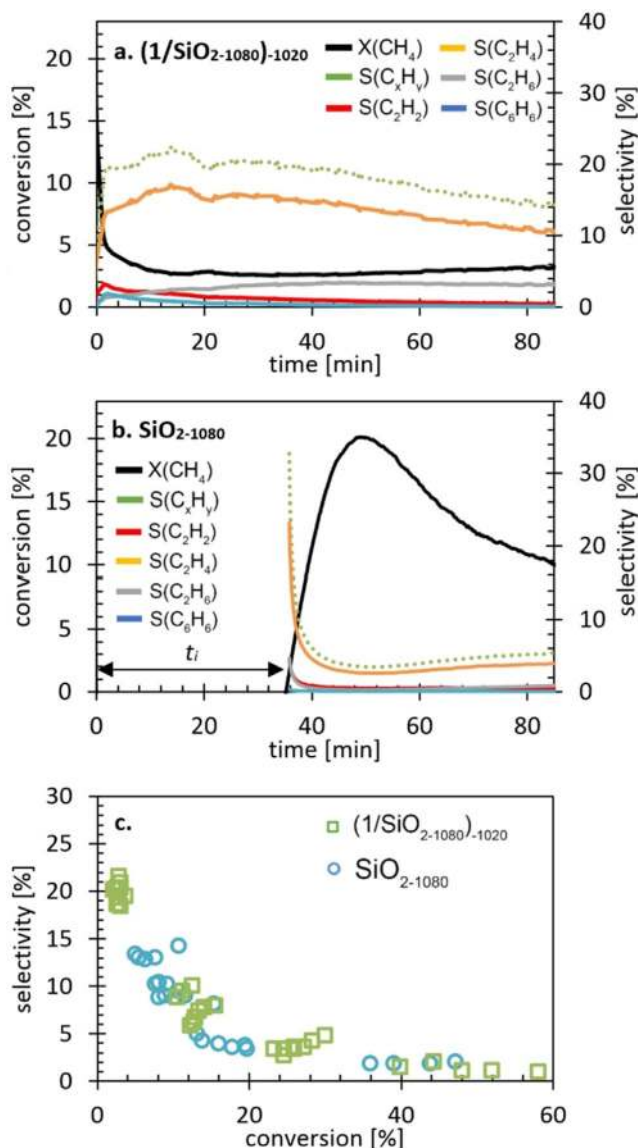


Figure 2. Relative distribution of the hydrocarbons in the gas phase at different conversion levels at 10 and 20 min for (a) (1/SiO₂₋₁₀₈₀)-1020 and (b) SiO₂₋₁₀₈₀. The conversion was controlled by changing the flow of the reactive gas. (c) Conversion-selectivity plot for both compounds constructed from the first 20 min of NOCM experiments with different contact times.

In summary, we have demonstrated that the combined SOMC/TMPs approach enables the preparation of a high surface area silica with Fe^{II} single sites, even after a thermolysis at 1020 °C. The synthesized material promotes non-oxidative coupling of CH₄ to higher hydrocarbons (C₂H₆, C₂H₄, C₂H₂, C₆H₆), reaching a selectivity of 20% at 3% conversion. However, the Fe^{II} sites quickly reduce and form carburized Fe⁰ nanoparticles. This is accompanied by the deposition of coke, the formation of surface hydrosilanes and paramagnetic defects. This contrasts with the reactivity of silica dehydroxylated at 1080 °C that favours, after an induction period, the formation of carbon deposits, rather than hydrocarbons. This indicates that iron sites selectively suppress the surface reactivity and improve the selectivity.

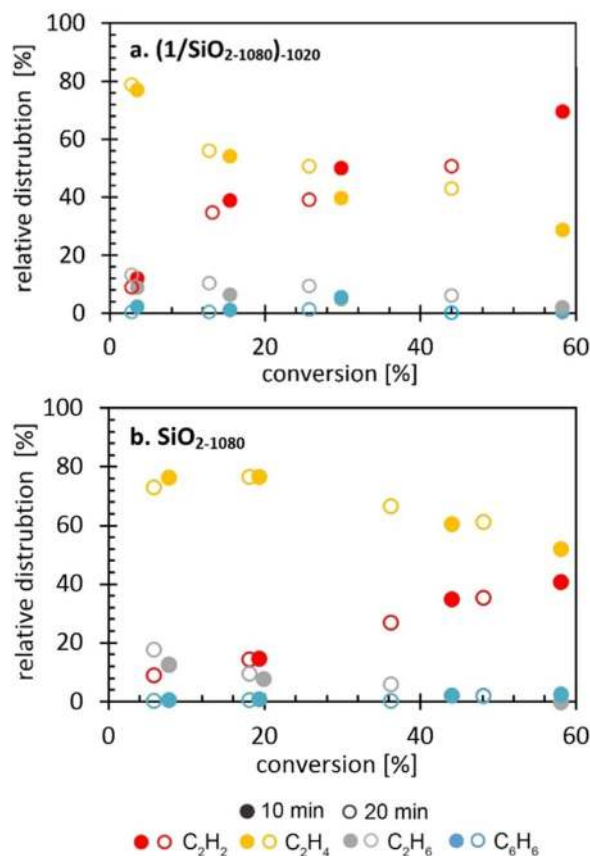


Figure 3. Relative distribution of the hydrocarbons in the gas phase at different conversion levels at 10 and 20 min for (a) (1/SiO₂₋₁₀₈₀)-1020 and (b) SiO₂₋₁₀₈₀. The conversion was controlled by changing the flow of the reactive gas.

Acknowledgements

Dr. P. Šot and Dr. M. A. Newton thank to Shell Global Solutions International B.V. for financial help. We acknowledge European Synchrotron Research Facility for awarded beamtimes CH 5647, CH-5585 at beamlines ID26 and BM25. We thank Swiss Light Source for a provided beamtime 20170821 at SuperXAS. We thank Dr. D. Degler, Dr. R. G. Castro, Dr. O. V. Safonova, J. Meyet, A. J. Knorpp and Dr. J. A. Mendéz-Burak for provided support at beamlines, Dr. M. P. Conley for help with the crystallography, and Prof. Dr. M. Bröring (Institut für Anorganische und Analytische Chemie) and Prof. Dr. F. J. Litterst (Institut für Physik der Kondensierten Materie) at TU Braunschweig for providing access to the SQUID magnetometer and Mössbauer spectrometer. We thank Dr. F. Krumeich (ETHZ) for electron microscopy.

Conflict of interest

The authors declare no conflict of interest.

Keywords: catalysis · C–H activation · iron · methane · silica

- [1] a) P. Schwach, X. Pan, X. Bao, *Chem. Rev.* **2017**, *117*, 8497–8520; b) P. Tang, Q. Zhu, Z. Wu, D. Ma, *Energy Environ. Sci.* **2014**, *7*, 2580–2591; c) N. D. Parkyns, C. I. Warburton, J. D. Wilson, *Catal. Today* **1993**, *18*, 385–442; d) M. C. Alvarez-Galvan, N. Mota, M. Ojeda, S. Rojas, R. M. Navarro, J. L. G. Fierro, *Catal. Today* **2011**, *171*, 15–23.
- [2] C. Guéret, M. Daroux, F. Billaud, *Chem. Eng. Sci.* **1997**, *52*, 815.
- [3] a) A. Galadima, O. Muraza, *J. Ind. Eng. Chem.* **2016**, *37*, 1–13; b) J. H. Lunsford, *Angew. Chem. Int. Ed. Engl.* **1995**, *34*, 970–980; *Angew. Chem.* **1995**, *107*, 1059–1070; c) G. E. Keller, M. M. Bhasin, *J. Catal.* **1982**, *73*, 9–19.
- [4] a) P. Xie, T. Pu, A. Nie, S. Hwang, S. C. Purdy, W. Yu, D. Su, J. T. Miller, C. Wang, *ACS Catal.* **2018**, *8*, 4044–4048; b) X. Guo, G. Fang, G. Li, H. Ma, H. Fan, L. Yu, C. Ma, X. Wu, D. Deng, M. Wei, D. Tan, R. Si, S. Zhang, J. Li, L. Sun, Z. Tang, X. Pan, X. Bao, *Science* **2014**, *344*, 616–619; c) S. J. Han, S. Lee, H. W. Kim, S. K. Kim, Y. T. Kim, *ACS Catal.* **2019**, *9*, 7984–7997; d) M. Sakbodin, Y. Wu, S. C. Oh, E. D. Wachsman, D. Liu, *Angew. Chem. Int. Ed.* **2016**, *55*, 16149–16152; *Angew. Chem.* **2016**, *128*, 16383–16386; e) S. C. Oh, E. Schulman, J. Zhang, J. Fan, Y. Pan, J. Meng, D. Liu, *Angew. Chem. Int. Ed.* **2019**, *58*, 7083–7086; *Angew. Chem.* **2019**, *131*, 7157–7160.
- [5] a) J. J. Spivey, G. Hutchings, *Chem. Soc. Rev.* **2014**, *43*, 792–803; b) I. Vollmer, N. Kosinov, Á. Szécsényi, G. Li, I. Yarulina, E. Abou-Hamad, A. Gurinov, S. Ould-Chikh, A. Aguilar-Tapia, J.-L. Hazemann, E. Pidko, F. Hensen, F. Kapteijn, J. Gascon, *J. Catal.* **2019**, *370*, 321–331; c) B. M. Weckhuysen, D. Wang, M. P. Rosynek, J. H. Lunsford, *Angew. Chem. Int. Ed. Engl.* **1997**, *36*, 2374–2376; *Angew. Chem.* **1997**, *109*, 2471–2473.
- [6] a) L. B. Avdeeva, T. V. Reshetenko, Z. R. Ismagilov, V. A. Likhobolov, *Appl. Catal. A* **2002**, *228*, 53–63; b) M. A. Ermakova, D. Y. Ermakov, A. L. Chuvilin, G. G. Kuvshinov, *J. Catal.* **2001**, *201*, 183–197; c) A. A. Ibrahim, A. H. Fakeeha, A. S. Al-Fatesh, A. E. Abasaheed, W. U. Khan, *Int. J. Hydrogen Energy* **2015**, *40*, 7593–7600; d) M. A. Ermakova, D. Y. Ermakov, *Catal. Today* **2002**, *77*, 225–235; e) D. P. Serrano, J. A. Botas, P. Pizarro, I. Moreno, G. Gómez, *Int. J. Hydrogen Energy* **2015**, *40*, 5237–5243.
- [7] a) C. Copéret, A. Comas-Vives, M. P. Conley, D. P. Estes, A. Fedorov, V. Mougél, H. Nagae, F. Núñez-Zarur, P. A. Zhizhko, *Chem. Rev.* **2016**, *116*, 323–421; b) J. D. A. Pelletier, J.-M. Basset, *Acc. Chem. Res.* **2016**, *49*, 664–677; c) S. L. Wegener, T. J. Marks, P. C. Stair, *Acc. Chem. Res.* **2012**, *45*, 206–214.
- [8] a) K. L. Furdala, T. D. Tilley, *J. Catal.* **2003**, *216*, 265–275; b) K. L. Furdala, R. L. Brutchey, T. D. Tilley in *Surface and Interfacial Organometallic Chemistry and Catalysis* (Eds.: C. Copéret, B. Chaudret), Springer, Heidelberg, **2005**, pp. 69–115.
- [9] C. Copéret, *Acc. Chem. Res.* **2019**, *52*, 1697–1708.
- [10] M. F. Delley, M.-C. Silaghi, F. Nuñez-Zarur, K. V. Kovtunov, O. G. Salnikov, D. P. Estes, I. V. Koptuyug, A. Comas-Vives, C. Copéret, *Organometallics* **2017**, *36*, 234–244.
- [11] K. Searles, G. Siddiqi, O. V. Safonova, C. Copéret, *Chem. Sci.* **2017**, *8*, 2661–2666.
- [12] J. Meyet, K. Searles, M. A. Newton, M. Wörle, A. P. van Bavel, A. D. Horton, J. A. van Bokhoven, C. Copéret, *Angew. Chem. Int. Ed.* **2019**, *58*, 9841–9845; *Angew. Chem.* **2019**, *131*, 9946–9950.
- [13] A. W. Holland, G. Li, A. M. Shahin, G. J. Long, A. T. Bell, T. D. Tilley, *J. Catal.* **2005**, *235*, 150–163.
- [14] S. L. Scott, J.-M. Basset, *J. Am. Chem. Soc.* **1994**, *116*, 12069–12070.
- [15] M. Wilke, F. Farges, P.-E. Petit, J. G. E. Brown, F. Martin, *Am. Mineral.* **2001**, *86*, 714–730.
- [16] P. Šot, C. Copéret, J. A. van Bokhoven, *J. Phys. Chem. C* **2019**, *123*, 23480–23487.
- [17] S. Janbroers, J. N. Louwen, H. W. Zandbergen, P. J. Kooyman, *J. Catal.* **2009**, *268*, 235–242.
- [18] J. Chipman, *Metall. Mater. Trans. B* **1972**, *3*, 55–64.
- [19] a) G. Ennas, A. Musinu, G. Piccaluga, D. Zedda, D. Gatteschi, C. Sangregorio, J. L. Stanger, G. Concas, G. Spano, *Chem. Mater.* **1998**, *10*, 495–502; b) N. A. Ivanova, A. A. Onischuk, S. V. Vosel, P. A. Purtov, N. T. Vasev, V. F. Anufrienko, V. N. Ikorski, *Appl. Magn. Reson.* **2008**, *33*, 285; c) T. Fun-Dow, S. L. Manatt, S. I. Chan, *Geochim. Cosmochim. Acta* **1973**, *37*, 1201–1211.
- [20] a) D. Savchenko, A. Vasin, S. Muto, E. Kalabukhova, A. Nazarov, *Phys. Status Solidi B* **2018**, *255*, 1700559; b) V. A. Radzig, A. A. Ischenko, *Kinet. Catal.* **2011**, *52*, 316–329.
- [21] a) J. M. Buriak, *Chem. Mater.* **2014**, *26*, 763–772; b) D. G. Permenov, V. A. Radzig, *Kinet. Catal.* **2004**, *45*, 14–23; c) N. Muradov, *Catal. Commun.* **2001**, *2*, 89–94.

Manuscript received: March 5, 2020

Accepted manuscript online: March 10, 2020

Version of record online: June 9, 2020